JOURNAL OF APPLIED CRYSTALLOGRAPHY

ISSN 1600-5767

Received 5 January 2016
Accepted 29 July 2016

Edited by V. Holý, Charles University, Prague, Czech Republic

Keywords: *PyNX.Ptycho*; ptychography; X-ray coherent diffraction imaging; nanostructures.

PyNX.Ptycho: a computing library for X-ray coherent diffraction imaging of nanostructures

Ondřej Mandula,[a,b,c,d] Marta Elzo Aizarna,[b,c,d] Joël Eymery,[c,d] Manfred Burghammer[b] and Vincent Favre-Nicolin[b,c,d,e]*

[a]Fondation Nanosciences, Grenoble, France, [b]ESRF – The European Synchrotron, 38043 Grenoble Cedex 9, France, [c]Université Grenoble Alpes, INAC-SP2M, F-38000 Grenoble, France, [d]CEA, INAC-SP2M, F-38000 Grenoble, France, and [e]Institut Universitaire de France, Paris, France. *Correspondence e-mail: favre@esrf.fr

X-ray imaging techniques have undergone a remarkable development during the past decade, taking advantage of coherent X-ray sources. Among these techniques, ptychography allows reconstruction of the specimen and the illumination probe from a series of diffraction patterns without any prior knowledge about the sample. However, the reconstruction of the ptychographic data remains challenging and the reconstruction software is often not publicly available. Presented here is an open-source library for the reconstruction of two-dimensional ptychographic data, written in Python. This library implements existing algorithms, with examples of data reconstruction on both simulated and experimental (Bragg ptychography on heterogeneous strained InAs/GaAs nanowires) data sets. It can be used for educational (simulation) purposes or experimental data analysis, and also features an OpenCL version of the ptychography algorithm for high-performance computing.

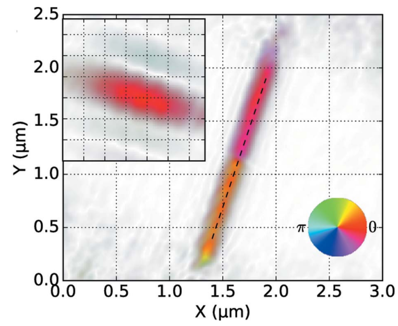

1. Introduction

X-ray imaging is a family of techniques popular in materials and biological science. Its high penetration depth, sensitivity to the local perturbations of the crystalline lattice (when in Bragg geometry) and sub-micrometre resolution make X-ray imaging the method of choice for non-invasive visualization of the specimen interior: see reviews by Robinson & Harder (2009), Sakdinawat & Attwood (2010) and Thibault *et al.* (2014).

X-ray coherent diffraction imaging (CDI) exploits the coherent properties of the X-ray beam to estimate the complex scattering density of the specimen from the recorded intensity of the far-field diffraction pattern by means of phase retrieval algorithms (Miao *et al.*, 1999; Livet, 2007; Robinson & Harder, 2009).

Interpretation of the complex scattering density depends on the geometry of the CDI experiment (Chapman & Nugent, 2010). The morphology of the specimen can be studied in the forward scattering geometry, displayed in Fig. 1(*a*). The sample is illuminated with a coherent X-ray beam and the scattered exit wave is recorded with a pixel detector placed on the axis of the incoming beam. The insertion of a beam stop might be necessary to protect the detector from the direct undiffracted beam. However, blocking of the low spatial frequencies causes difficulty in the reconstruction process (Marchesini *et al.*, 2003).

Crystalline samples can also be studied in the Bragg geometry, represented in Fig. 1(*b*), recording the diffraction pattern of a particular Bragg peak. It can be shown that, while the amplitude of the recovered complex density corresponds to the morphology of the crystal, the phase is sensitive to the local displacement of the crystal lattice (Pfeifer *et al.*, 2006; Newton *et al.*, 2010). The non-invasive mapping of the strain field makes Bragg CDI a unique tool for studying a variety of problems in strained nanomaterials with a number of applications in electronics and photonics (Favre-Nicolin *et al.*, 2010; Newton *et al.*, 2010; Haag *et al.*, 2013).

Ptychography is a CDI method using multiple diffraction patterns from overlapping areas of the sample (Hoppe, 1969; Rodenburg & Bates, 1992; Rodenburg *et al.*, 2007; Thibault *et al.*, 2008). The redundancy due to overlaps facilitates the inversion of the diffraction patterns. The combination of CDI with scanning also allows imaging of extended objects with dimensions larger than the size of the beam or the transverse coherence length of the source. In contrast with single-frame CDI techniques, ptychography can also recover the illumination probe (Thibault *et al.*, 2009; Maiden & Rodenburg, 2009). Ptychography algorithms reconstruct the object and the beam consistently with all diffraction patterns. The consistency in the overlapping regions represents the real-space constraint and the method allows recovery of the complex scattering density without *a priori* knowledge about the object or probe. Ptychography can be performed both in the forward scattering geometry, showing the morphology of the specimen (Thibault *et al.*, 2008; Giewekemeyer *et al.*, 2010; Dierolf *et al.*, 2010; Wilke *et al.*, 2012; Diaz *et al.*, 2012), and in the Bragg geometry, which is sensitive to the strain (Godard *et al.*, 2011; Huang *et al.*, 2012; Hruszkewycz *et al.*, 2012; Takahashi *et al.*, 2013; Chamard *et al.*, 2015).

Despite the increasing popularity of ptychography, the reconstruction algorithms are often not shared. Several software packages for ptychography analysis already exist [*e.g. PtyPy* (Enders & Thibault, 2014) and parallel ptychography (Nashed *et al.*, 2014)], including advanced data analysis such as reconstruction of state mixtures for the treatment of partial coherence (Thibault & Menzel, 2013). However, for various reasons beyond the scope of this article, the corresponding code is not always publicly available.

The purpose of this article is to demonstrate our open-source code for two-dimensional ptychographic reconstruction on experimental and simulated data and make it available for further development in the community. We make clear and explicit all the parameters of the reconstruction and show one specific implementation that can be compared and tested against. Establishing a robust and transparent reconstruction procedure is highly desirable for further development and a wider application of ptychography among non-specialist research groups, as well as for the education of young researchers.

This article is organized as follows: in §2 we will discuss algorithms for ptychography, and in §3 we present our open-source library *PyNX.Ptycho* for ptychographic reconstruction, with examples of experimental and simulated data evaluation in §4.

2. Algorithms for reconstruction of ptychographic data

Following Thibault *et al.* (2008), we assume that the recorded intensity of the jth diffraction pattern of the ptychographic data set can be described as

$$I(\mathbf{q}, \mathbf{d}_j) = \left|\mathcal{F}\left\{P(\mathbf{r} - \mathbf{d}_j)O(\mathbf{r})\right\}\right|^2, \qquad (1)$$

where the complex valued object $O(\mathbf{r})$ is multiplied with a complex valued probe $P(\mathbf{r})$ shifted to the position $\mathbf{d}_j$ in the sample (direct) space. $\mathcal{F}$ denotes a Fourier transform (or other propagation function) with respect to the direct-space coordinate $\mathbf{r}$, and $\mathbf{q}$ is the reciprocal-space coordinate. The outcoming wavefront, described by the product $\psi(\mathbf{r}, \mathbf{d}_j) = P(\mathbf{r} - d_j)O(\mathbf{r})$, is an approximation valid for thin specimens (Thibault *et al.*, 2008).

Rodenburg & Bates (1992) proposed the Wigner distribution deconvolution approach to solve equation (1) analytically for $O(\mathbf{r})$. This approach, demonstrated by Chapman (1996), assumes detailed knowledge of the probe $P(\mathbf{r})$ and requires Nyqvist sampling of the Wigner distribution both in reciprocal space $\mathbf{q}$ and in translations $\mathbf{d}_j$, because the translation steps determine the pixel size of the recovered object $O(\mathbf{r})$. Large data sets are needed to image extended objects, which makes this approach impractical.

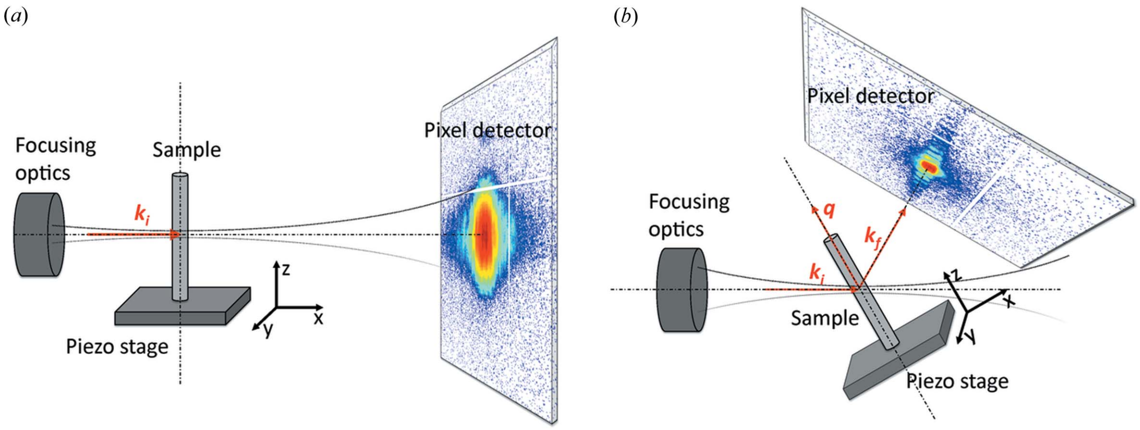

Figure 1
The geometry of the CDI experiment (not drawn to scale). Only a coherent part of the incoming beam is used. (*a*) The forward scattering geometry for morphological studies of the specimen. (*b*) The Bragg geometry for mapping the displacement of the crystal lattice in the direction of the Bragg peak $\mathbf{q}$.

The ptychographic iterative engine (PIE), solving equation (1) iteratively, has been proposed by Faulkner & Rodenburg (2004). The iterative approach relaxes the sampling requirement on the translations $\mathbf{d}_j$, facilitating the experiment. Moreover, Thibault *et al.* (2008) presented a method based on the difference map (DM) algorithm, demonstrating that not only the object $O(\mathbf{r})$ but also the probe $P(\mathbf{r})$ can be iteratively recovered from the ptychographic data. The extended PIE (ePIE) capable of reconstructing both object and probe followed soon after (Maiden & Rodenburg, 2009). The possibility of simultaneous object and probe reconstruction was an important step towards wider applicability of the method and gave rise to new and interesting applications of ptychography as a beam characterization method (Schropp *et al.*, 2013).

The general scheme of the iterative approach is based on the Gerchberg–Saxton procedure used for the standard (single-frame) CDI (Gerchberg & Saxton, 1972), where the complex valued diffraction pattern is computed from the current estimate of the object and probe *via* a propagation function, typically a Fourier transform. The constraints in reciprocal space are imposed by replacing the intensity of the calculated diffraction pattern $I^{\rm calc}(\mathbf{q}, \mathbf{d}_j)$ with the measured values $I^{\rm obs}(\mathbf{q}, \mathbf{d}_j)$. The real-space constraints are introduced through the consistency within the overlapping areas.

Currently, the ePIE and DM represent the two main groups of ptychographic algorithms. Schematic views of the algorithms' cores are shown in Fig. 2. The ePIE can be regarded as a Fienup hybrid input–output algorithm adapted to the series of ptychographic measurements, *i.e.* using an overlap constraint in direct space rather than a support constraint. The ePIE contains an inner cycle over the measured diffraction patterns [red loop in Fig. 2(*a*)]. In each cycle only one diffraction pattern is used to update the corresponding part of the object. The data are used sequentially, updating one specific part of the object, determined by each position step, at a time. The inner cycle terminates when all the measured data have been used. The outer iterative loop [black lines in Fig. 2(*a*)] runs until convergence has been reached. The updates of the object can be alternated with a symmetrical update of the probe.

The DM contains a single iterative cycle, where all the measured diffraction patterns are used to update the whole object and/or probe in one step, maintaining the consistency of the current estimate with all measured data. In other words, the object (and probe) updates use information from all the measurements in parallel. In our view this is a more efficient way of exploiting the data and in our experience this algorithm performs better when the initial probe estimate is not accurate.

Equation (1) can also be tackled *via* direct optimization of the object and probe (Guizar-Sicairos & Fienup, 2008; Thibault & Guizar-Sicairos, 2012; Godard *et al.*, 2012). The complex values of $O(\mathbf{r})$ and $P(\mathbf{r})$ can be varied systematically to maximize the 'similarity' between the calculated and measured diffraction patterns. From the statistical point of view, this can be formulated as maximizing the log-likelihood of our model [equation (1)] considering the noise statistics of the measured data (Bishop, 2006).

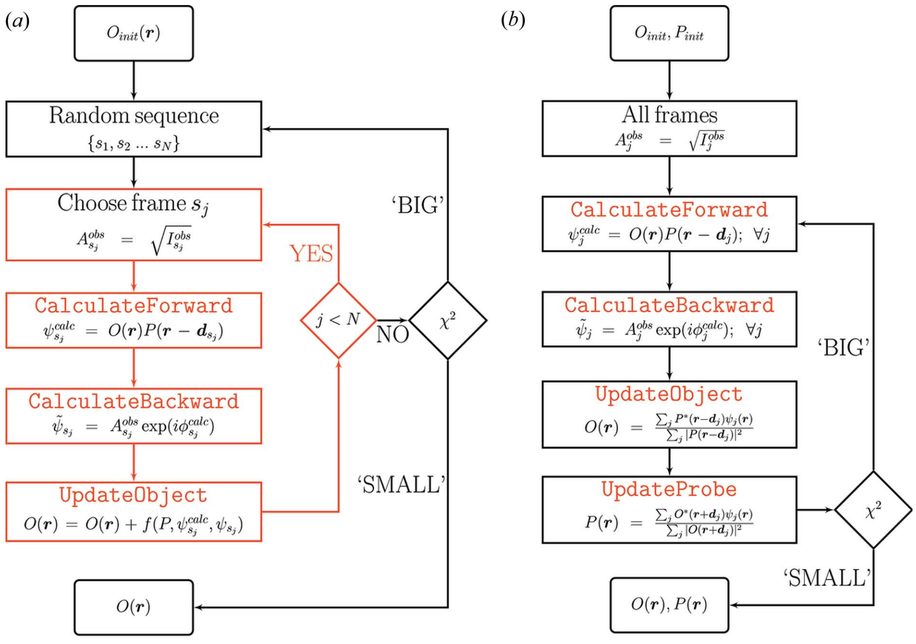
(*a*)
$O_{init}(\boldsymbol{r})$
Random sequence
$\{s_1, s_2 \dots s_N\}$
Choose frame s_j
$A^{obs}_{s_j} = \sqrt{I^{obs}_{s_j}}$
CalculateForward
$\psi^{calc}_{s_j} = O(\boldsymbol{r})P(\boldsymbol{r} - \boldsymbol{d}_{s_j})$
CalculateBackward
$\tilde{\psi}_{s_j} = A^{obs}_{s_j} \exp(i\phi^{calc}_{s_j})$
UpdateObject
$O(\boldsymbol{r}) = O(\boldsymbol{r}) + f(P, \psi^{calc}_{s_j}, \psi_{s_j})$
YES
$j < N$
NO
χ^2
'BIG'
'SMALL'
$O(\boldsymbol{r})$
(*b*)
O_{init}, P_{init}
All frames
$A^{obs}_j = \sqrt{I^{obs}_j}$
CalculateForward
$\psi^{calc}_j = O(\boldsymbol{r})P(\boldsymbol{r} - \boldsymbol{d}_j);\ \forall j$
CalculateBackward
$\tilde{\psi}_j = A^{obs}_j \exp(i\phi^{calc}_j);\ \forall j$
UpdateObject
$O(\boldsymbol{r}) = \frac{\sum_j P^*(\boldsymbol{r}-\boldsymbol{d}_j)\psi_j(\boldsymbol{r})}{\sum_j |P(\boldsymbol{r}-\boldsymbol{d}_j)|^2}$
UpdateProbe
$P(\boldsymbol{r}) = \frac{\sum_j O^*(\boldsymbol{r}+\boldsymbol{d}_j)\psi_j(\boldsymbol{r})}{\sum_j |O(\boldsymbol{r}+\boldsymbol{d}_j)|^2}$
'BIG'
χ^2
'SMALL'
$O(\boldsymbol{r}), P(\boldsymbol{r})$

$$f(X, \psi^{calc}_{s_j}, \psi_{s_j}) = \alpha_X \frac{X^*(\boldsymbol{r} - \boldsymbol{d}_{s_j})}{|X(\boldsymbol{r} - \boldsymbol{d}_{s_j})|^2_{max}} \left(\psi_{s_j} - \psi^{calc}_{s_j}\right)$$

Figure 2
Schematic views of the cores of the ptychography algorithms. $O(\mathbf{r})$ and $P(\mathbf{r})$ denote the complex valued object and probe, respectively. $A^{\rm obs}$ are the measured amplitudes obtained as the square root of the measured diffraction intensity $I^{\rm obs}$. The text in red shows the names of the functions called in our reconstruction algorithm. (*a*) The ePIE using the data sequentially, with an inner (red) loop iterating over all diffraction patterns. The probe can be recovered using the symmetrical scheme [$P(\mathbf{r})$ exchanged with $O(\mathbf{r})$]. (*b*) The DM algorithm, using all measured data in parallel.

For Gaussian noise, maximizing the log-likelihood is equivalent to the minimization of the square differences in all pixels in reciprocal space:

$$R_{\rm G} = \sum_{\mathbf{q}} \left[I^{\rm calc}(\mathbf{q}) - I^{\rm obs}(\mathbf{q})\right]^2. \quad (2)$$

For Poisson noise the expression to be minimized is

$$R_{\rm P} = \sum_{\mathbf{q}} \left[I^{\rm calc}(\mathbf{q}) - I^{\rm obs}(\mathbf{q}) \log I^{\rm calc}(\mathbf{q})\right]. \quad (3)$$

The difference between the two objective functions is significant for low photon counts in the pixel detector (less than 100 counts), where the Poisson noise approach is more appropriate for photon-counting detectors (Godard *et al.*, 2012).

Direct minimization of the experimental data has to be performed with care. An enhancement of high spatial frequencies resulting in 'grainy' images has been observed (Thibault & Guizar-Sicairos, 2012). A regularization term related to Good's roughness penalty (Verveer, 1998) can be added to the log-likelihood term to achieve 'smoother' results (Guizar-Sicairos & Fienup, 2008):

$$Q(\mathbf{r}) = \sum_{\mathbf{r}} \left|O(\mathbf{r}) - O(\mathbf{r} \pm \Delta_x)\right|^2 + \left|O(\mathbf{r}) - O(\mathbf{r} \pm \Delta_y)\right|^2, \quad (4)$$

with Δ_x and Δ_y the shift of one pixel in the x or y direction, respectively.

The cost function to be minimized is then

$$C(O, P) = R(O, P) + \alpha Q(O), \quad (5)$$

with an empirical constant α governing the 'smoothness' of the results. The derivatives $\partial C/\partial O$ and $\partial C/\partial P$ can be written analytically for both the Gaussian and the Poisson case and efficient minimization procedures such as conjugate gradient descent (Nocedal & Wright, 2006) are readily available (Jones *et al.*, 2015). Note that this minimization, while it involves more floating point operations, is not excessively expensive when using OpenCL, only requiring twice the amount of time per cycle compared with the ptychography algorithm, probably because OpenCL calculations are often limited by memory transfers rather than floating point operations. However, because it is a direct minimization, it cannot get out of local minima, and is best suited to the final refinement of already good estimates of $O(\mathbf{r})$ and $P(\mathbf{r})$ (Marchesini, 2007; Thibault & Guizar-Sicairos, 2012).

The positions of each individual scan can be subject to an experimental error, producing artefacts in the reconstruction. Similar to the direct optimization of the object and probe, the positions of the individual scans $\mathbf{d}_j$ can be refined within the maximum-likelihood framework, minimizing R as a function of $\mathbf{d}_j$ (Guizar-Sicairos & Fienup, 2008), although different strategies have been proposed (Zhang *et al.*, 2013). The lack of an analytical expression for spatial derivatives of $O(\mathbf{r})$ and $P(\mathbf{r})$ prevents the use of a conjugate gradient, so we use the Powell conjugate direction minimization method (Powell, 1964; Jones *et al.*, 2015) to minimize R as a function of $\mathbf{d}_j$. The minimization procedure can be alternated with updates of O and P to accommodate the results for the optimized positions.

In general, the iterative reconstruction remains challenging owing to the fine-tuning of parameters hidden in the algorithms. The object and probe update functions of the ePIE and DM algorithms are nonlinear with many local minima (Marchesini, 2007). The final result depends strongly on many factors, including the initial values, the reconstruction parameters and the specific implementation of the algorithm. To our knowledge, there are no convergence proofs available for either method. A transparent and explicit specification of all the reconstruction parameters is necessary for a reproducible reconstruction.

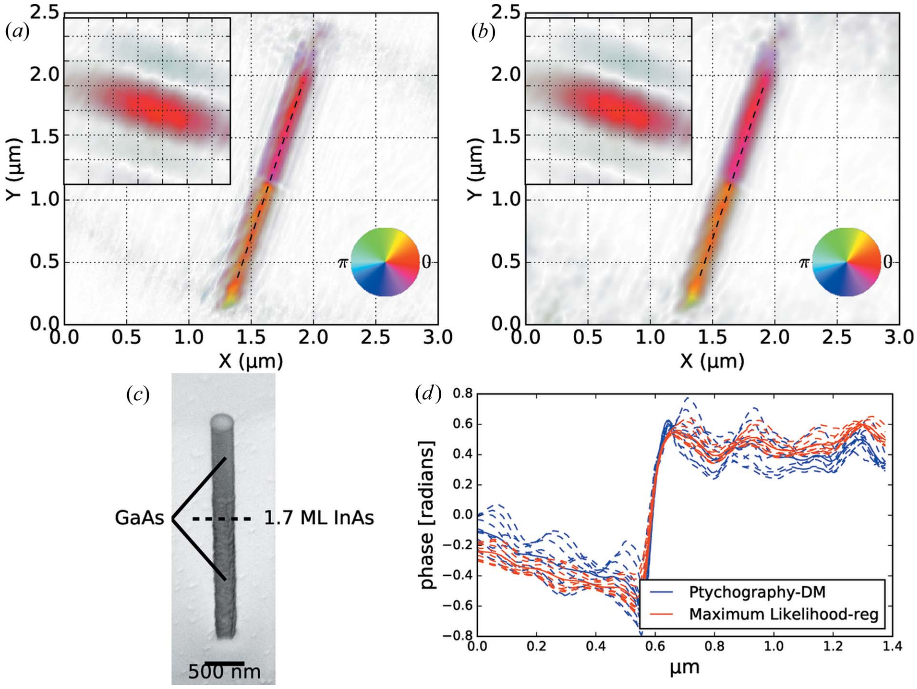

Figure 3
(*a*) A ptychographic reconstruction of a GaAs nanowire with an ~1.7 monolayer InAs insertion in Bragg geometry for the (113) reflection. The brightness corresponds to the amplitude and the colour to the phase of the complex image. The reconstructed probe (using the same colour scheme) is shown in the top-left inset. (*b*) The same object and probe after a maximum-likelihood optimization using a regularization constant, penalizing local variations in the complex object density. (*c*) An electron microscopy image of the GaAs nanowire with the 1.7 monolayer of InAs indicated schematically. (*d*) Profiles of the phase along the nanowire, as indicated with dashed lines in parts (*a*) and (*b*) using line interpolation, before (blue) and after (red) maximum-likelihood optimization. Pixel values along ten neighbouring pixel rows are plotted with dashed lines and the averages in solid lines. Note the smaller spread of the phase values after the maximum-likelihood minimization using regularization.

3. Implementation and availability

We implemented the DM (Thibault *et al.*, 2009) ptychography algorithm and the direct minimization procedures (Thibault & Guizar-Sicairos, 2012) in the Python programming language as a part of the *PyNX* open-source library (Favre-Nicolin *et al.*, 2011). The ePIE was also implemented but was less robust and has been removed owing to possible legal issues. This software is now distributed by the ESRF on its web site (http://ftp.esrf.fr/pub/scisoft/PyNX/).

The *PyNX.Ptycho* module contains reconstruction algorithms, and tools for the simulation of ptychographic data and visualization of the results. An example experimental data set, and scripts for simulation and evaluation, are also provided.

The module requires the standard scientific Python libraries (*matplotlib*, *scipy*, *numpy*) (Hunter, 2007; Jones *et al.*, 2015; Dubois *et al.*, 1996). The Fourier transform, as the core of the reconstruction, is optionally computed using the FFTW algorithm (*fftw3f* library; Frigo & Johnson, 2005) for faster calculations.

An OpenCL implementation of the DM algorithm is also proposed, and allows faster optimization (5× to 30× acceleration compared with the FFTW approach, depending on hardware) using a graphical processing unit [see Nashed *et al.* (2014) for a review of ptychography using graphical processing units (GPUs)]. In this approach, all the data are loaded and prepared in Python, and the different steps of the algorithm are executed entirely on the GPU to avoid slow memory transfers. The code uses *PyOpenCL* (Klöckner *et al.*, 2012) for simpler (on-the-fly) handling of data transfer and kernel compilation, and the *gpyfft* (https://github.com/geggo/gpyfft) and *clFFT* (https://github.com/clMathLibraries/clFFT) libraries for OpenCL FFT.

This implementation requires ~0.26 s per ptychography cycle (object and probe update) for a data set with 1000 frames with 336 × 336 pixels, using a single-threaded Python program running on a 3.4 GHz Intel Xeon E5-2643 and a single nVidia GTX Titan X graphics card. Only 1 GB of memory out of the 12 GB available on the GPU are used in this case, so larger data sets (larger detectors or number of frames) could be analysed.

Two other modules (not presented in detail in this article) are included in the *PyNX* library and can also be used for coherent X-ray imaging:

(i) `pynx.wavefield`, which can be used for wavefield propagation (using either CPU or OpenCL implementation) in the near- and far-field regimes, and which can also use a fractional Fourier transform (García *et al.*, 1996; Mas *et al.*, 1999) approach for a continuous transform from near to far field.

(ii) `pynx.clFZP`, which can be employed for calculation (also using OpenCL) of the wavefield produced by a Fresnel zone plate illuminated coherently from a point source, either using a full (disc) or a rectangular illumination, and taking into account a central stop and order-sorting aperture. This code could easily be specialized to compute the illumination from any type of two-dimensional phase object which can be defined by an analytical function of the position in the lens plane.

4. Examples

Several examples are included in the *PyNX* software package to demonstrate the ptychographic reconstruction.

4.1. Reconstruction of experimental data

In this section we show a reconstruction of a GaAs nanowire with a 1.7 monolayer of InAs inserted at half height (Fig. 3*c*). The ptychographic data set was acquired on the ESRF beamline ID01. An X-ray beam (E = 8.7 keV) was focused with a partially illuminated Fresnel zone plate (fully coherent illumination) on the nanowire. In total, 114 diffraction patterns (336 × 336 pixels after cropping) were recorded with a Maxipix pixel detector (Ponchut *et al.*, 2007) in the Bragg configuration for the (113) reflection of GaAs. The scan positions were placed along the Archimedean spiral (described by $r = b\theta$, with r being the length of the position vector under the angle θ, and b controlling the distance between successive turns). Steps of 200 nm were used along the spiral with 25 s per frame exposure. The diffraction data and the positions of the ptychographic scan and the initial object and probe are saved in `pynx/Examples/Data/`.

It should be noted that, for this example, we do not take into account the specific case of the Bragg geometry: in a small-angle ptychography experiment, the sample-to-detector direction is parallel to the incident beam and perpendicular to the sample displacement during the scan, so that the algorithm only uses a two-dimensionnal projection of the three-dimensional object and the incoming X-ray probe. In Bragg geometry, the incident probe makes an angle with the sample-to-detector line and is not perpendicular to the sample displacement plane. Therefore, the description of ptychography scattering as the multiplication of two-dimensional fields corresponding to the sample and the probe, both perpendicular to the propagation direction, is an approximation. However, because the sample is thin (diameter ~200 nm) and the Bragg angle remains small ($\theta \simeq 23^\circ$), the algorithm works and yields a two-dimensional projection of the sample and probe. A more complete treatment (using either three-dimensional ptychography or two-dimensional back-projection) is beyond the scope of this article and has already been proposed (Godard *et al.*, 2011; Huang *et al.*, 2012; Hruszkewycz *et al.*, 2012; Takahashi *et al.*, 2013; Chamard *et al.*, 2015).

We used the DM algorithm (Thibault *et al.*, 2009) to recover the complex density of both the nanowire and the probe. The reconstruction presented in this section was calculated with the script `Examples/exper_113.py`. The reconstruction can be executed with the following code running 100 iterations of the DM algorithm of Fig. 2(*b*) updating only the object, followed by 400 iterations of DM updating both object and probe:

```
from pynx import ptycho
# Reading experimental data
data = load('Data/data_113.npz')
ampl = sqrt(data['iobs']) # the data are intensities

# Positions of the scans
posx, posy = data['posx'], data['posy']

# Initial object (random) and probe (Gaussian)
obj0 = data['obj0']
probe0 = data['probe0']

gpu = "Titan" # Use OpenCL for faster calculation

#Initialize Ptycho2D object
p = ptycho.Ptycho2D(amplitudes=ampl,
  positions=(posx, posy), probe0=probe0, obj0=obj0)
```

```
# Run 100 cycles updating object only
p.CL_Run(100, updateProbe=False, opencl_device=gpu)

# 400 cycles updating object and probe
p.CL_Run(400, updateProbe=True, opencl_device=gpu)
```

The result of the reconstruction (with the phase gradient corrected for the centring of the diffraction pattern) is shown in Fig. 3(*a*). For our computer (Intel Xeon CPU E5-2643 at 3.40 GHz with an nVidia Titan X GPU card for OpenCL computing) the 500 cycles take approximately 16 s. Note that the wavelength and detector distance can optionally be given (λz parameter) to take into account the quadratic phase term of the far-field diffraction.

After the initial convergence of the algorithm, the results can be further refined within the maximum-likelihood framework. The command

```
p.CL_ML_Poisson(100, reg_fac=reg_fac,
updateObject=True, updateProbe=True,
opencl_device=gpu)
```

invokes direct minimization of the objective function [equation (5)] with respect to the object. The regularization constant α in equation (5) is set by the parameter `reg_fac`. We use Poisson statistics for this minimization, although the difference from Gaussian statistics is very low in this case ($\sim 10^6$ photons per frame) [see Godard *et al.* (2012) and Thibault & Guizar-Sicairos (2012) for discussions of noise models in ptychography]. The result of the regularized direct minimization (100 cycles without regularization and 100 with, requiring an additional 15 s of execution) is shown in Fig. 3(*b*).

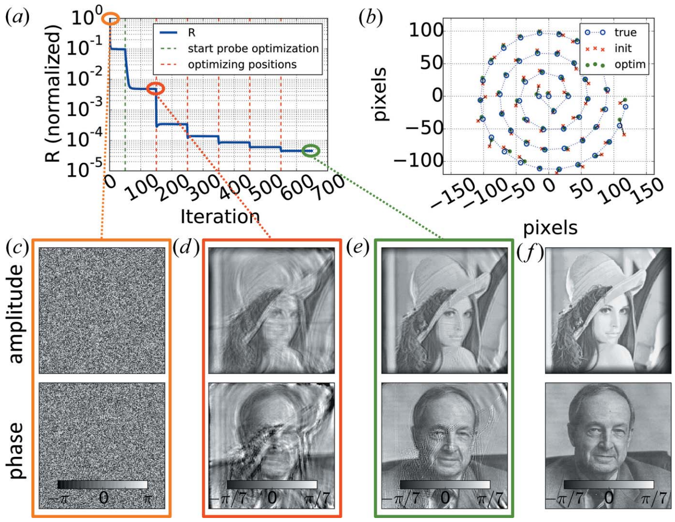

Figure 4
Evaluation of the simulated data with error in scan positions. (*a*) The convergence curve. The first 50 iterations optimize the object only. The vertical green dashed line indicates the start of the optimization of both object and probe. Optimization of the scan positions starts at iteration 150. Vertical red dashed lines mark the positions of the optimization procedure (every 50 iterations from iteration 150). (*b*) Refinement of the scan positions. True values are shown as blue circles, initial randomly displaced values as red crosses and optimized positions as green circles. (*c*)–(*f*) The amplitude (top) and phase (bottom) of (*c*) the initial object, (*d*) the reconstructed object with incorrect positions and (*e*) the result after the scan positions optimization procedure. (*f*) The true object used for the simulation.

Note that the regularization term [equation (4)] can induce a small degradation of the resolution as it corresponds to a term penalizing local variations in the object complex density (Thibault & Guizar-Sicairos, 2012). Therefore, it should be tuned for every optimization to reduce noise without significantly affecting the resolution. However, the regularization should be regarded as a guide towards a smoother solution which remains consistent with the measured data, rather than a simple smoothing of the results – this is a compromise between the best possible resolution and *a priori* restraints for the model (where strong pixel-to-pixel phase/strain changes are often not physical). The required smoothness can be controlled by the parameter α in equation (5). In our case, the loss of resolution is barely visible [a slight decrease in the phase slope near the InAs insertion position in Fig. 3(*d*)].

There is a jump in the phase of approximately 1 radian in the centre of the nanowire (see Fig. 3*d*). This discontinuity indicates the displacement of the crystal lattice by 0.27 Å in the direction of the (113) scattering vector and corresponds to the insertion of the InAs layer in this position.

4.2. Simulation of the ptychographic data set

Simulated ptychographic data are invaluable for testing the algorithm performance. Our software contains a simulation tool for generating ptychographic data from an arbitrary complex valued object and probe. Simulated intensity diffraction patterns are corrupted with Poisson noise.

The script `Examples/simul_refinePos.py` demonstrates the simulation of the ptychographic data set from an object with the amplitude and phase set to two different photographs (Fig. 4*f*). The reconstruction algorithm was supplied with deliberately randomly displaced scan positions (red crosses in Fig. 4*b*). The object was initialized with a random amplitude and phase (see Fig. 4*c*), while the probe was initialized with a Gaussian, different from the true probe. The reconstructed object after 150 iterations of the DM algorithm (the first 50 iterations not updating the probe) is shown in Fig. 4(*d*). The amplitude and phase are severely distorted because of the incorrect scan positions. The refinement within the maximum-likelihood framework (Guizar-Sicairos & Fienup, 2008) iteratively corrects the scan positions and is alternated with 100 iterations of the DM algorithm to accommodate the object and probe to the new scan positions. The convergence curve of this procedure shows distinctive steps, as seen in Fig. 4(*a*). The improvement of the reconstructed object is apparent in Fig. 4(*e*); however, an imprint of the amplitude remains in the phase image. This is partly due to the un-structured probe (in our case an anisotropic Gaussian). Simulation with a disc probe [as used in the simulations by Zhang *et al.* (2013)] results in better refined images (see `Examples/simul_discProbe_refinePos.py`), but a smooth Gaussian probe is closer to the reality of the measurement with a focused beam. The refined scan positions are plotted as green circles in Fig. 4(*b*), showing a significant reduction in the displacement error.

5. Conclusions

In this article we have presented our open-source Python library *PyNX.Ptycho* for two-dimensional ptychographic reconstruction, and several examples of analysis on experimental and simulated data sets. We have also discussed refinement of the results within the maximum-likelihood framework and shown how some experimental parameters, such as scan positions, can be corrected with an iterative minimization procedure. All results presented in this paper can be reproduced with the evaluation scripts and experimental data included in the *PyNX* package.

Acknowledgements

This work was partially supported by the French ANR XDISPE (grant No. ANR-11-JS10-004-01) and by the Fondation Nanosciences (Grenoble, France) in the framework of the Chair of Excellence of Professor Jian Min Zuo. The authors thank Peter Boesecke and other ESRF ID01 staff for help with experimental data acquisition. We would also like to thank Jean-Luc Rouvière and Robert McLeod for stimulating discussions.

References

Bishop, C. M. (2006). *Pattern Recognition and Machine Learning.* Heidelberg: Springer.

Chamard, V., Allain, M., Godard, P., Talneau, A., Patriarche, G. & Burghammer, M. (2015). *Sci. Rep.* **5**, 9827.

Chapman, H. N. (1996). *Ultramicroscopy*, **66**, 153–172.

Chapman, H. N. & Nugent, K. (2010). *Nat. Photon.* **4**, 833–839.

Diaz, A., Trtik, P., Guizar-Sicairos, M., Menzel, A., Thibault, P. & Bunk, O. (2012). *Phys. Rev. B*, **85**, 020104.

Dierolf, M., Thibault, P., Menzel, A., Kewish, C. M., Jefimovs, K., Schlichting, I., von König, K., Bunk, O. & Pfeiffer, F. (2010). *New J. Phys.* **12**, 035017.

Dubois, P. F. *et al.* (1996). *Comput. Phys.* **10**, 262–267.

Enders, B. & Thibault, P. (2014). *Ptypy – Ptychography Reconstruction for Python*, http://dx.doi.org/10.5281/zenodo.12480.

Faulkner, H. & Rodenburg, J. (2004). *Phys. Rev. Lett.* **93**, 023903.

Favre-Nicolin, V., Coraux, J., Richard, M.-I. & Renevier, H. (2011). *J. Appl. Cryst.* **44**, 635–640.

Favre-Nicolin, V., Mastropietro, F., Eymery, J., Camacho, D., Niquet, Y. M., Borg, B. M., Messing, M. E., Wernersson, L.-E., Algra, R. E., Bakkers, E. P. A. M., Metzger, T. H., Harder, R. & Robinson, I. K. (2010). *New J. Phys.* **12**, 035013.

Frigo, M. & Johnson, S. G. (2005). *Proc. IEEE*, **93**, 216–231.

García, J., Mas, D. & Dorsch, R. G. (1996). *Appl. Opt.* **35**, 7013–7018.

Gerchberg, R. & Saxton, W. (1972). *Optik*, **35**, 237–246.

Giewekemeyer, K., Thibault, P., Kalbfleisch, S., Beerlink, A., Kewish, C. M., Dierolf, M., Pfeiffer, F. & Salditt, T. (2010). *Proc. Natl Acad. Sci. USA*, **107**, 529–534.

Godard, P., Allain, M., Chamard, V. & Rodenburg, J. (2012). *Opt. Express*, **20**, 25914–25934.

Godard, P., Carbone, G., Allain, M., Mastropietro, F., Chen, G., Capello, L., Diaz, A., Metzger, T. H., Stangl, J. & Chamard, V. (2011). *Nat. Commun.* **2**, 568.

Guizar-Sicairos, M. & Fienup, J. R. (2008). *Opt. Express*, **16**, 7264–7278.

Haag, S. T., Richard, M.-I., Welzel, U., Favre-Nicolin, V., Balmes, O., Richter, G., Mittemeijer, E. J. & Thomas, O. (2013). *Nano Lett.* **13**, 1883–1889.

Hoppe, W. (1969). *Acta Cryst.* A**25**, 495–501.

Hruszkewycz, S. O., Holt, M. V., Murray, C. E., Bruley, J., Holt, J., Tripathi, A., Shpyrko, O. G., McNulty, I., Highland, M. J. & Fuoss, P. H. (2012). *Nano Lett.* **12**, 5148–5154.

Huang, X., Harder, R., Leake, S., Clark, J. & Robinson, I. (2012). *J. Appl. Cryst.* **45**, 778–784.

Hunter, J. D. *et al.* (2007). *Comput. Sci. Eng.* **9**, 90–95.

Jones, E. *et al.* (2015). *SciPy: Open-source Scientific Tools for Python*, http://www.scipy.org/.

Klöckner, A., Pinto, N., Lee, Y., Catanzaro, B., Ivanov, P. & Fasih, A. (2012). *Parallel Comput.* **38**, 157–174.

Livet, F. (2007). *Acta Cryst.* A**63**, 87–107.

Maiden, A. M. & Rodenburg, J. M. (2009). *Ultramicroscopy*, **109**, 1256–1262.

Marchesini, S. (2007). *Rev. Sci. Instrum.* **78**, 011301.

Marchesini, S., He, H., Chapman, H. N., Hau-Riege, S. P., Noy, A., Howells, M. R., Weierstall, U. & Spence, J. C. H. (2003). *Phys. Rev. B*, **68**, 140101.

Mas, D., Garcia, J., Ferreira, C., Bernardo, L. M. & Marinho, F. (1999). *Opt. Commun.* **164**, 233–245.

Miao, J., Charalambous, P., Kirz, J. & Sayre, D. (1999). *Nature*, **400**, 342–344.

Nashed, Y. S. G., Vine, D. J., Peterka, T., Deng, J., Ross, R. & Jacobsen, C. (2014). *Opt. Express*, **22**, 32082–32097.

Newton, M. C., Leake, S. J., Harder, R. & Robinson, I. K. (2010). *Nat. Mater.* **9**, 120–124.

Nocedal, J. & Wright, S. J. (2006). *Numerical Optimization*, 2nd ed., pp. 101–134. New York: Springer-Verlag.

Pfeifer, M. A., Williams, G. J., Vartanyants, I. A., Harder, R. & Robinson, I. K. (2006). *Nature*, **442**, 63–66.

Ponchut, C., Clément, J., Rigal, J. M., Papillon, E., Vallerga, J., LaMarra, D. & Mikulec, B. (2007). *Nucl. Instrum. Methods Phys. Res. Sect. A*, **576**, 109–112.

Powell, M. J. (1964). *Comput. J.* **7**, 155–162.

Robinson, I. & Harder, R. (2009). *Nat. Mater.* **8**, 291–298.

Rodenburg, J. M. & Bates, R. H. T. (1992). *Philos. Trans. R. Soc. London Ser. A*, **339**, 521–553.

Rodenburg, J. M., Hurst, A. C., Cullis, A. G., Dobson, B. R., Pfeiffer, F., Bunk, O., David, C., Jefimovs, K. & Johnson, I. (2007). *Phys. Rev. Lett.* **98**, 034801.

Sakdinawat, A. & Attwood, D. (2010). *Nat. Photon.* **4**, 840–848.

Schropp, A., Hoppe, R., Meier, V., Patommel, J., Seiboth, F., Lee, H. J., Nagler, B., Galtier, E. C., Arnold, B., Zastrau, U., Hastings, J. B., Nilsson, D., Uhlén, F., Vogt, U., Hertz, H. M. & Schroer, C. G. (2013). *Sci. Rep.* **3**, 1633.

Takahashi, Y., Suzuki, A., Furutaku, S., Yamauchi, K., Kohmura, Y. & Ishikawa, T. (2013). *Phys. Rev. B*, **87**, 121201.

Thibault, P., Dierolf, M., Bunk, O., Menzel, A. & Pfeiffer, F. (2009). *Ultramicroscopy*, **109**, 338–343.

Thibault, P., Dierolf, M., Menzel, A., Bunk, O., David, C. & Pfeiffer, F. (2008). *Science*, **321**, 379–382.

Thibault, P. & Guizar-Sicairos, M. (2012). *New J. Phys.* **14**, 063004.

Thibault, P., Guizar-Sicairos, M. & Menzel, A. (2014). *J. Synchrotron Rad.* **21**, 1011–1018.

Thibault, P. & Menzel, A. (2013). *Nature*, **494**, 68–71.

Verveer, P. J. (1998). PhD thesis, Technische Universiteit Delft, The Netherlands.

Wilke, R. N., Priebe, M., Bartels, M., Giewekemeyer, K., Diaz, A., Karvinen, P. & Salditt, T. (2012). *Opt. Express*, **20**, 19232–19254.

Zhang, F., Peterson, I., Vila-Comamala, J., Diaz, A., Berenguer, F., Bean, R., Chen, B., Menzel, A., Robinson, I. K. & Rodenburg, J. M. (2013). *Opt. Express*, **21**, 13592–13606.